

ON THE MODELLING OF MOISTURE TRANSPORT IN AIR AND CAPILLARY POROUS MATERIALS

Van Belleghem M. ^{*,a}, De Backer L. ^b, Janssens A. ^b, De Paepe M. ^a

^{*}Author for correspondence

^aDepartment of Flow, Heat and Combustion Mechanics,

^bDepartment of Architecture and Urban Planning,

Ghent University,

Ghent, 9000,

Belgium,

E-mail: marnix.vanbelleghem@ugent.be

ABSTRACT

Accurate modelling of coupled heat and moisture transport problems in capillary porous materials and the interaction with surrounding air is important for many applications going from wetting and drying of soils to convective drying in industrial dryers. In this study the emphasis lies on the modelling of convective drying of porous building materials with a capillary or hygroscopic-capillary nature. An important aspect for the correct modelling of convective drying is the way the air boundary is implemented. Most modelling approaches today use convective transfer coefficients to model the impact of convective flow over a porous material. Often the heat and mass analogy is used to calculate a convective mass transfer coefficient (found in literature or from CFD calculations) from the convective heat transfer coefficient. A wrong estimation of transfer coefficients can however have a significant impact on the modelling outcome.

This paper gives a short overview of the state of the art in conjugate heat and mass transport modelling for convective drying. In this review shortcomings of currently applied modelling approaches are highlighted.

Secondly a finite volume coupled heat and moisture transport model is discussed. Recently this heat and moisture transport model was implemented in a commercial CFD package to model the coupled transport in porous materials and air. The material model is validated using a drying experiment on ceramic brick. This model is then used to study the importance of correct boundary conditions for convective drying modelling.

NOMENCLATURE

C	[J/kgK]	Heat capacity
C_b	[W/m ² K ⁴]	Stefan-Boltzmann constant
d	[m]	Thickness
D	[m ² /s]	Vapour diffusivity

E	[J]	Total energy
g	[kg/m ² s]	Mass flux
h	[W/m ² K]	Heat transfer coefficient
h_m	[kg/s]	Mass transfer coefficient
K_l	[s]	Liquid permeability
L	[J/kg]	Latent heat
M	[kg/mol]	Molar mass
p	[Pa]	Pressure
q	[W/m ²]	Heat flux
R	[J/molK]	Universal gas constant
R_v	[J/kgK]	Specific gas constant water vapour
RH	[-]	Relative humidity
Sc	[-]	Schmidt number
t	[s]	Time
T	[°C]	Temperature
v	[m/s]	Velocity
w	[kg/m ³]	Moisture content
x	[m]	Distance
Y	[-]	Mass fraction

Special characters

ϵ	[-]	Emissivity
λ	[W/mK]	Thermal conductivity
μ	[-]	Vapour resistance factor
ν	[m ² /s]	Kinematic viscosity
φ	[-]	Open porosity
ρ	[kg/m ³]	Density

Subscripts

a	Air
$a+v$	Humid air
e	Environment, climate chamber
eff	effective
l	Liquid
mat	Material
$PMMA$	Polymethyl methacrylate
rad	Radiation
$roof$	Roof
s	Surface
sat	Saturation
$turb$	Turbulent
v	vapour
XPS	Extruded polystyrene

INTRODUCTION: MODELLING CONVECTIVE DRYING

For the convective drying studied in this paper, the dried medium is a porous material (hygroscopic and/or porous active) and the drying medium is (moist) air. There is a wide range of literature available that studies the interaction of a wet porous material and the surrounding air. This section will only give a brief overview of models found in literature and does not have the ambition to be in any way complete. More complete overviews of drying models can be found in [1] and [2].

In the large collection of available models two groups can be distinguished: analytical models and numerical models. Analytical models are often confined to 1D models and are often limited to simple cases. For example the diffusivity is considered constant [3] or the drying is considered isothermal [4]. The applied boundary conditions are fixed temperature and humidity at the boundary (Dirichlet (first-type) boundary conditions), fixed fluxes at the boundaries (Neumann (second-type) boundary conditions) or fixed transfer coefficients (Robin (third-type) boundary conditions) [4-6]. Only boundary conditions of the third type can be used to model convective drying. If more complex boundary conditions are present, like spatially and/or temporally varying boundary conditions, 1D models do no longer suffice and most often numerical models have to be used.

Numerical convective drying models can be subdivided into two main categories, depending on how the interaction with the drying medium (often air) is modelled. The first category of models uses transfer coefficients to model the convective heat and mass transfer. A second category of models uses a conjugated approach. Momentum, heat and mass transport in the air is solved simultaneously with the heat and mass transport in the porous material.

When numerical models are used there is still a vast group of models that apply constant transfer coefficients at the boundary [e.g. 7-10]. These coefficients are often taken from experimental correlations.

Some authors state that the use of a constant transfer coefficient is incorrect when a developing boundary layer is present [11,12]. In this case it is necessary to use spatially varying transfer coefficients. The boundary layer for heat and mass will be thinner at the leading edge of a wet surface that is dried. This will result in higher transfer coefficient at this leading edge. As a result the moisture and temperature distribution in the material will be two or even three dimensional.

The most advanced convective drying models today solve the heat, mass and momentum equation simultaneously [13-15]. The conditions of the drying medium flowing over the porous material determine the drying rate of the porous material while the surface conditions of the porous material determine the heat and moisture distribution in the drying medium (air). It can however be stated that the impact of this modelling approach is limited when forced convection is present. The time scale of the convection problem solved in the air is much smaller than that of the drying process. However for natural convection the impact of simultaneous modelling of air and material could be more important. In this case the convection in the air is strongly determined by the material boundary conditions. Setting a fixed

boundary condition at the material (fixed transfer coefficient) would thus not correspond with reality.

It is clear from this discussion that there is still some uncertainty on how boundary conditions should be implemented in drying models. Therefore a more thorough study of the impact of boundary conditions on a drying model outcome is needed. In the present paper only forced convection is considered. The drying model discussed in the next section assumes steady air conditions which allow to take the transfer coefficients invariable in time. A finite volume drying model is developed and validated with experiments found in literature. The impact of the different boundary condition implementations is investigated and discussed. First a 1D model with constant transfer coefficients is solved, next a 2D model with spatially varying transfer coefficients and finally a 3D model.

HEAT, AIR AND MOISTURE MODEL

In this section the used heat, air and moisture (HAM) model is discussed. Three phases can be distinguished in a porous material:

- Gas phase: air and water vapour
- Liquid phase: liquid water
- Solid phase: material matrix

It is possible to model the different phases separately on a micro scale and subsequently integrate over the total material volume to obtain the macro scale heat and moisture transport [16]. This would however require such a detailed knowledge of the pore structure of the material that this approach is not feasible for materials encountered in practice. Therefore a phenomenological approach on a macro scale [17] was used for the derivation of the transport equations. In these transport equations the material is considered to be a continuum. By consequence macro heterogenic effects like cracks can not be simulated while the effects of micro heterogeneities are averaged over the calculation element.

Two conservation equations can be deduced, conservation of mass and conservation of energy, both for the air and the porous material. This section will only give a short overview of the deduced equations and their meaning. A more detailed explanation of these equations is found in [18,19].

Moisture is transported in air through a combination of convection and diffusion. In the air no liquid moisture is transported only water vapour. The water vapour diffusion flux is represented by g (kg/m²s) and is assumed proportional to the gradient of the water vapour mass fraction.

$$\frac{\partial(\rho_{a+v}Y)}{\partial t} + \nabla \cdot (\bar{v}\rho_{a+v}Y) = -\nabla \cdot \bar{g} = \nabla \cdot (\rho_{a+v}D_{eff}\nabla Y) \quad (1)$$

Y is the mass fraction of water vapour in air (kg_v/kg_{v+a}), ρ_{v+a} is the total air density, v is the velocity of air. D_{eff} (m²/s) is the sum of the molecular and turbulent vapour diffusion coefficient (Eq. (2)).

$$D_{eff} = D_{va} + D_{turb}$$

$$D_{va} = 2.31 \times 10^{-5} \frac{101325}{p} \left(\frac{T}{273.16} \right)^{1.81} \quad (2)$$

$$D_{turb} = \frac{v_{turb}}{Sc_{turb}}$$

p (Pa) is the operating pressure and T the temperature (K). The turbulent diffusion coefficient is given as the ratio of the turbulent kinematic viscosity v_{turb} (m²/s) to the turbulent Schmidt number Sc_{turb} (-). The value used for the turbulent Schmidt number is 0.7.

The air is modelled as incompressible. This is an acceptable assumption since the encountered air velocities in buildings are low and much smaller than the speed of sound. However the density does depend on temperature and vapour concentrations. The density is calculated with Eq. (3).

$$\rho_{a+v} = \frac{p}{RT \left(\frac{Y}{M_v} + \frac{1-Y}{M_a} \right)} \quad (3)$$

Here R is the universal gas constant (J/molK), M_v and M_a the molar weight of vapour and dry air respectively (kg/mol).

In air the energy transport equation can be written as a combination of storage, convection and diffusion of latent and sensible heat. For the temperature ranges encountered in this work the latent heat of water vapour can be assumed constant. This results in the following equation for the energy balance in the air:

$$\frac{\partial(\rho_{v+a} CT)}{\partial t} + \nabla \cdot [\bar{v}(\rho_{v+a} CT)] = \nabla \cdot [\lambda_{eff} \nabla T - (C_v - C_a) \bar{g} T] \quad (4)$$

In this equation C_v (J/kgK) is the heat capacity of water vapour and C_a (J/kgK) the heat capacity of air, T (K) is the temperature, v is the air velocity and λ_{eff} (W/mK) is the effective heat conductivity. The effective heat conductivity is the sum of the molecular heat conductivity λ and the turbulent conductivity λ_{turb} . The turbulent conductivity is calculated from the turbulent kinematic viscosity v_{turb} and the turbulent Prandtl number with Eq. (5).

$$\lambda_{turb} = \rho_{a+v} C \frac{v_{turb}}{Pr_{turb}} \quad (5)$$

$$\lambda_{eff} = \lambda + \lambda_{turb}$$

The mass weighted average heat capacity C is given by Eq. (6).

$$C = Y C_v + (1 - Y) C_a \quad (6)$$

The following values have been used for the different material properties: $C_v = 1875.2$ J/kgK, $C_a = 1006.43$ J/kgK, $\lambda = 0.0257$ W/mK, $Pr_{turb} = 0.85$.

Moisture transport in a hygroscopic capillary porous material can be attributed to two transport mechanisms: vapour transport described by Fick's law (Eq. (7)) and liquid transport described by Darcy's law (Eq. (8)).

$$\bar{g}_v = \frac{D_{va}}{\mu R_v T} \nabla p_v \quad (7)$$

$$\bar{g}_l = -K_l \nabla p_c \quad (8)$$

μ (-) is the water vapour resistance factor which is the ratio of the water vapour diffusion coefficient in still air to the diffusion coefficient in the porous material. K_l (s) is the liquid permeability and p_c (Pa) is the capillary pressure, \bar{g}_v the vapour flux (kg/m²s) and \bar{g}_l the liquid water flux (kg/m²s).

The change of the total moisture content in time of a control volume of porous material is in other words due to moisture flux leaving the control volume and moisture flux going into the volume. This can be expressed in differential form by Eq. (9).

$$\frac{\partial w}{\partial p_c} \frac{\partial p_c}{\partial t} = \nabla \cdot \left[K_l \nabla p_c + \frac{D_{va}}{\mu} \frac{\rho_v}{\rho_l R_v T} \nabla p_c + \left(p_{sat} \frac{\partial RH}{\partial T} + RH \frac{\partial p_{sat}}{\partial T} \right) \nabla T \right] \quad (9)$$

The vapour pressure p_v in Eq. (7) was transformed to the capillary pressure p_c using Kelvin's law (Eq. (10)).

$$p_c = \rho_l R_v T \ln RH \quad (10)$$

The relative humidity RH is defined by Eq. (11) and the saturation vapour pressure p_{sat} is assumed only dependant on the temperature (Eq. (12)).

$$RH = \frac{p_v}{p_{sat}} \quad (11)$$

$$p_{sat} = 611 \exp\left(\frac{17.08(T - 273.15)}{T - 38.97}\right) \quad (12)$$

$\partial w / \partial p_c$ represents the moisture capacity and can be determined from the moisture retention curve $w(p_c)$ which gives the moisture content as a function of the capillary pressure.

Similar to the mass transport in a porous material also heat transport is only due to diffusion. Transport due to convection is neglected. Eq. (13) represents the heat conservation equation in a porous material. Heat is transported through the porous material due to heat conduction, sensible heat transported together with the liquid transport and sensible and latent heat transported together with the vapour diffusion.

$$\frac{\partial E}{\partial t} = (\rho_{mat} C_{mat} + w_l C_l + w_v C_v) \frac{\partial T}{\partial t} + C_l T \frac{\partial w_l}{\partial t} + (C_v T + L) \frac{\partial w_v}{\partial t} = \nabla \cdot [\lambda_{mat} \nabla T - C_l T \vec{g}_l - (C_v T + L) \vec{g}_v] \quad (13)$$

In Eq. (13) λ_{mat} (W/mK) is the heat conductivity of the porous material. This conductivity is a function of the moisture content of the porous material since moisture contained inside the porous material would result in an increase of the conductivity. ρ_{mat} (kg/m³) is the density of the porous material and C_{mat} is the heat capacity of the porous material. L is the latent heat of evaporation and is taken as a constant (2.5e6 J/kg). C_v and C_l are the heat capacities of vapour and liquid water respectively and are again assumed constant ($C_v= 1875.2$ J/kgK, $C_l= 4192.1$ J/kgK).

The total moisture content w (kg/m³) can be divided into the liquid moisture content w_l and the vapour moisture content w_v . Both are linked with the total moisture content through the open porosity ψ (-).

$$w_l = \frac{\psi - w}{\frac{1}{\rho_l} - \frac{1}{\rho_v}} \quad w_v = \frac{w - \psi}{\frac{1}{\rho_l} - \frac{1}{\rho_v}} \quad (14)$$

MODEL VALIDATION: SETUP DESCRIPTION

This section gives a short description of the experimental setup used in this paper to validate the HAM model described in the previous section. The experiment was performed by Defraeye [20] and his results are used here for the validation. A schematic representation of the test setup is given in Figure 1. In this experiment a sample of ceramic brick is dried by convection, by placing it in a wind tunnel. Dry air flows over the top side of the brick and the brick is dried out from one side, while the other sides are impermeable for moisture. Defraeye [20] constructed a small wind tunnel from transparent polymethyl methacrylate (PMMA) to perform convective drying experiments on building materials such as ceramic brick. Air is drawn in by a fan, passes over a flow straightener (honeycomb) and flows through a convergent section before entering the test section. Because of the high width to height ratio, the flow in the tunnel can be assumed two-dimensional. The open circuit wind tunnel was placed in a climate chamber where the mean temperature was set at 23.8°C (with a standard deviation of 0.2°C) and a mean relative humidity of 44% (with a standard deviation of 0.8%). The sample of ceramic brick was wetted and placed in the wind tunnel so that the top face of the sample becomes the bottom of the test section. The sample was wetted to a moisture content of 126kg/m³ which is approximately the capillary moisture content (130kg/m³). The sides of the sample were insulated with extruded polystyrene (XPS) and made impermeable for moisture. The velocity at the inlet of the test section and the turbulence intensity were measured with a PIV (particle image velocimetry) system. During the drying experiment temperatures at the side of the

ceramic brick were measured with thermocouples. Figure 1 shows the location of these thermocouples. In total 6 thermocouples were installed at a side wall. The temperature was measured at a depth of 10mm, 20mm and 30mm from the material-air interface and 10mm in the lower insulation (at 40mm from interface). To measure the inflow effect and the effect of a developing moisture and temperature boundary layer, a thermocouple was installed upstream of the centre thermocouples and downstream both at a depth of 10mm. The weight change of the test sample was continuously monitored by a balance. The sample of ceramic brick measuring 10mm by 10mm by 90mm, is placed in a container of plexiglass (PMMA). At the bottom of the container a layer of 20mm insulation (XPS) is installed. The front and back side of the container are covered with 15mm of insulation (XPS), the side walls of the brick sample are insulated with 30mm of XPS. The test section can be assumed symmetric along the x-axis since the flow in the channel was found to be two-dimensional [21]. The properties of the materials used in this paper are listed in Appendix A.

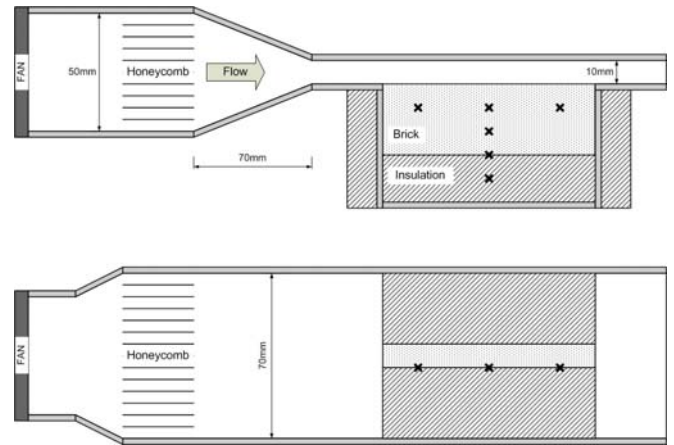


Figure 1 Schematic representation of the test section used by Defraeye [20]. x indicate the location of thermocouples.

MODEL VALIDATION: EFFECT OF BOUNDARY CONDITIONS

Modelling a cross section: constant transfer coefficients

First the setup in Figure 1 modelled by a 2D model representing a cross section of the setup. The heat and mass transfer coefficient along the surface are assumed constant for this case. The ceramic brick is surrounded by insulation material (XPS) and air flows over the brick at the top. All sides of the brick except the top are assumed impermeable for moisture. The heat transfer coefficient at the top of the brick was determined by CFD simulations performed for a 2D wind tunnel with constant surface temperature at the bottom. This resulted in a heat transfer coefficient as a function of the position in the duct. From this spatially varying transfer coefficient, an average value was determined of 22.5W/m²K. From the heat and mass analogy a mass transfer coefficient of 0.0258kg/m²s was

determined. The heat flux boundary condition of the remaining side surfaces is given by Eq. (15).

$$q = \frac{1}{\frac{1}{h_e} + \frac{d_{PMMA}}{\lambda_{PMMA}} + \frac{d_{XPS}}{\lambda_{XPS}}}(T_e - T_s) \quad (15)$$

λ_{XPS} and λ_{PMMA} are the heat conductivities of the insulation material and plexiglass respectively, h_e is the heat convection coefficient of the outside surfaces (excluding the top surface). This transfer coefficient is assumed constant and incorporates the effect of radiation from the surrounding. h_e was estimated at $8\text{W/m}^2\text{K}$ by Defraeye. The temperature of the surroundings, T_e was also constant and corresponded with the temperature of the climate chamber (23.8°C). Radiation at the interface brick-air was taken into account in a simplified way by assuming that the brick top face only sees the upper wall of the wind tunnel. This resulted in a view factor of 1. The temperature of the top wall of the wind tunnel, T_{roof} , was measured by Defraeye and an average value of 23.3°C was found. The radiative heat flux at the brick-air interface can be calculated according to [22] as:

$$q_{rad} = \frac{C_b}{\frac{1}{\varepsilon_1} + \frac{1}{\varepsilon_2} - 1}(T_{roof}^4 - T_s^4) \quad (16)$$

ε_1 and ε_2 are the emissivities for the roof and the brick surface respectively which are assumed to be 0.97 and 0.93. T_s is the surface temperature of the brick. C_b is the Stefan-Boltzmann constant ($5.67 \times 10^{-8}\text{W/m}^2\text{K}^4$). The boundary conditions at the top can be written as:

$$\begin{aligned} q &= h_a(T_a - T_s) + (L + C_v T_s)h_m(Y_a - Y_s) + q_{rad} \\ g &= h_m(Y_s - Y_a) \end{aligned} \quad (17)$$

The temperature in Eq. (17) is expressed in $^\circ\text{C}$. The second term on the right hand side incorporates the latent heat leaving the surface due to evaporation. Y_a is the mass fraction of the air entering the wind tunnel (corresponding with inlet temperature and relative humidity). Y_s is the mass fraction at the brick-air interface. For these simulations a grid of 200×20 cells was used. The grid was finer near the top. Figure 2 shows a comparison of the measurements performed by Defraeye [20] with the simulations for a 2D cross section of the brick. The figure shows the simulation results for adiabatic boundary conditions, for adiabatic boundary conditions with radiation at the top and for non-adiabatic boundary conditions. The temperature predicted during the CDR (constant drying rate) period is the wet bulb temperature (when adiabatic boundary conditions are assumed). Allowing a heat flow through the boundary walls and incorporating radiation from the top surface will alter the equilibrium temperature to a higher temperature. The temperature at a depth of 10mm in the brick is initially 23.8°C . Three periods during drying can be distinguished in the temperature course. First the temperature drops to the wet bulb temperature (in case of adiabatic side walls). This is the so

called decreasing drying rate period (DDRP) preceding the constant rate period (CDR). In this first transitional period there is an imbalance between the heat leaving the surface due to evaporation and heat supplied to the surface through convection. This causes the temperature to drop if the initial temperature is higher than the wet bulb temperature. If the temperature in the material reaches the wet bulb temperature, the heat flow from and to the surface is balanced and the temperature remains constant. This continues until drying out occurs at the surface. At that point the evaporation rate at the surface decreases and again an imbalance exist between the supplied heat and the heat leaving the surface. Less evaporation means that less latent heat is needed and the temperature at the surface will start to rise. This third drying period is called the falling rate period (FRP).

Radiation from the wind tunnel top wall to the brick-air interface will result in a higher equilibrium temperature at the brick surface. This temperature is slightly higher than the wet bulb temperature. By leaving the assumption that the side walls are adiabatic and allowing a heat flow through the insulation, the temperature at equilibrium will even further increase. Figure 2 also shows the measurements of the temperature at 10mm in the brick sample. The comparison with the simulations shows a clear underestimation by the simulations. Assuming that the simulations were performed accurately, this would indicate that the current model is underestimating the heat gains to the brick due to the introduced simplifications. The main simplifications here are the 2D modelling assumptions (neglecting 3D edge effect) and the constant transfer coefficients at the surface.

As more heat gains are allowed (radiation and heat gain through insulation), the equilibrium temperature rises and the constant drying rate period decreases. Figure 2 shows, for the simulated cases, how the constant drying rate period ends after 7 hours for the adiabatic case and after 5 hours for the non-adiabatic case. A higher temperature will result in a higher saturation mass fraction during the constant drying rate period and thus a higher evaporation rate. The brick will dry out faster. This is also depicted in Figure 3, which shows the scaled mass loss in time. This scaled mass loss is the ratio of the mass loss to the initial moisture content $(m_{w,init} - m_w)/m_{w,init}$. During the constant rate period the slope of this curve is constant and is a measure for the drying rate. The steeper slope for the non-adiabatic case indicates a higher drying rate which results in a faster decrease of the moisture content in the brick.

Due to the faster decrease in moisture content, the surface will dry out sooner and this in turn results in an earlier onset of the falling rate period. During the constant drying rate period, the drying rate is significantly higher than during the falling rate period. The drying rate is determined by outside transport conditions (convective transport in the air). When drying out at the surface occurs, the internal transport of water in the brick becomes the dominating mechanism.

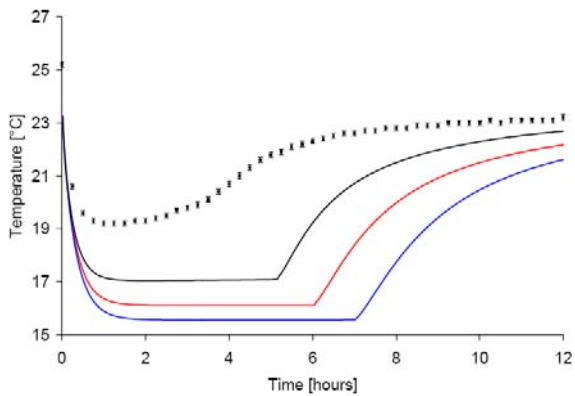


Figure 2 Temperature at a depth of 10mm, comparison between different boundary conditions: adiabatic sides and bottom (blue line), heat flux trough insulation (black line), adiabatic sides and bottom but radiation at top. Comparison with measurements by [20] (■).

This simplified 2D model allows to verify if the new model predicts the correct trends during drying. More specifically the different drying periods are reproduced by the model. It is however clear that the simplified model does not capture the boundary conditions accurate enough which results in an underestimation of the predicted temperatures.

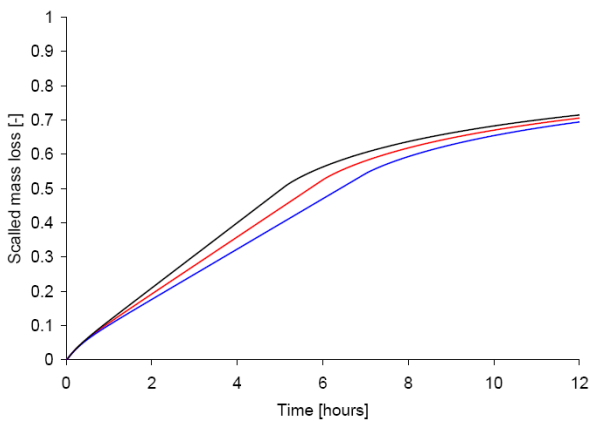


Figure 3 Scaled mass loss, comparison between different boundary conditions: adiabatic sides and bottom (blue line), heat flux trough insulation (black line), adiabatic sides and bottom but radiation at top.

Modelling a longitudinal section: developing boundary layer

As stated in the previous section, a 2D model of the cross section of a porous material subjected to convective drying is not able to fully grasp all the drying phenomena. One of the simplifications in the previous section was the use of constant transfer coefficients. This is only valid for a fully developed thermal and mass boundary layer. For developing boundary layers the heat and mass transfer coefficients will vary in space.

Heat and mass transfer at the leading edge of a sample subjected to convective drying will be higher since at this leading edge the boundary layers still have to develop and are still thin. This will result in a faster dryout at this leading edge and a distribution of temperature and moisture in the sample. In this section this leading edge effect is modelled and compared with simulations using constant transfer coefficients.

The convective transfer coefficients were determined using CFD simulations. Defraeye predicted the convective heat transfer coefficients in CFD by using a constant temperature boundary condition. The predicted heat transfer coefficient was then used to calculate the mass transfer coefficient using the Chilton-Colburn heat and mass analogy. Eq. (18) and (19) show the convection coefficients as a function of the position along the duct.

$$h(x) = 7.7577x^{-0.2958} \quad (18)$$

$$h_m(x) = \rho R_v T 5.514 \times 10^{-8} x^{-0.2958} \quad (19)$$

Figure 4 shows a comparison of the temperature at 10mm for a simulation of the cross section of a brick (see previous section) using average transfer coefficients and a simulation of the longitudinal section using spatially varying transfer coefficients. When a constant transfer coefficients is used, the graph shows an overestimation of the constant drying rate period. Drying out at the surface will occur sudden and equal over the entire surface. This results in an abrupt transition from constant drying rate period to falling rate period. If a growing boundary layer at the surface of the brick is considered, heat and mass transfer at the leading edge will be larger and dryout will start at that side. This results in parts of the surface being dried out while others are still wet. At the dry surface parts, heat convection to the surface will be higher than the latent heat leaving the surface, which results in a temperature rise at these zones. For the wet zones, the equilibrium temperature is still the wet bulb temperature. Due to the more gradual progression of the dryout at the surface, there is no longer a sudden transition between the different drying phases. The temperature in the brick will rise more gradually as is seen in Figure 4. From the measurements it can be seen that simulation of brick drying incorporating a developing boundary layer for heat and mass will predict the trends in drying more accurately. However, when comparing simulations with measurements it is clear that a correct prediction of the drying phenomena in a brick is only possible if all the boundary conditions are correctly implemented. This implies that a 3D simulation is necessary with a developing boundary layer at the top and non adiabatic boundary conditions at the sides.

3D Modelling of convective drying

For the 3D simulation of the setup in Figure 1, similar boundary conditions as in the previous sections are used. The heat losses through the sides are incorporated. The insulation and plexiglass surrounding the test sample were included in the computational domain. Still the air flow at the top of the sample was assumed 2D and the heat and mass transfer coefficients discussed in the previous section were used (Eq. (18) and (19)).

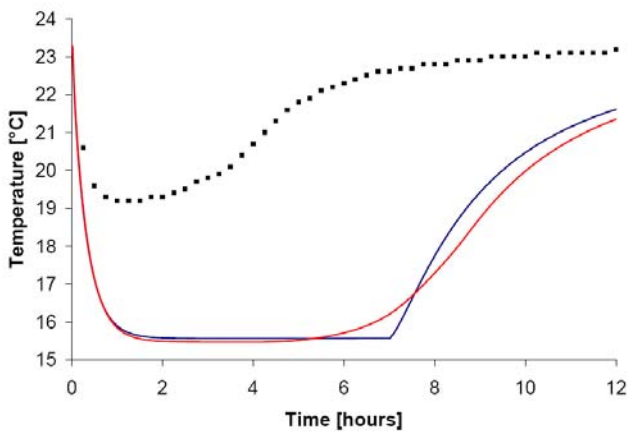


Figure 4 Simulation of the temperature at a depth of 10mm in ceramic brick using constant heat and mass transfer coefficients at the top (blue line) and spatially varying transfer coefficients (red line), comparison with measurements from [20] (■).

Graphs of the temperature evolution in the brick are reported in Figures 5-8. Temperature at a depth of 10mm, 20mm, 30mm (at the interface brick/insulation) and 40mm (10mm in the insulation) are compared with measurements. A measurement uncertainty of 0.1 °C is indicated in the figures. A good agreement between the model and the experiments was found. The largest deviations are found near the surface. The temperature at a depth of 10mm is slightly underestimated by the model. Also the onset of the falling rate period is delayed in the simulations. Nevertheless the equilibrium temperature (the lowest temperatures in Figure 6.16) is closely approximated by the model. Deeper in the material the approximation becomes even better. At a depth of 40mm (10mm in the insulation) the agreements is almost perfect. This indicates that the applied boundary conditions closely approach reality. Three main reasons for the deviations between the measurements and the simulations can be formulated. The first is the uncertainty in the material properties. This was also addressed by Defraeye [20] and similar studies were performed by Roels et al. [23] and Van Belleghem et al. [24]. Secondly there is an uncertainty on the implemented boundary conditions and initial conditions. The heat transfer coefficient at the side walls was not measured but estimated and the inlet temperature was taken constant, though in reality the temperature varied a little. The inlet velocity profile was measured using PIV but as stated by Defraeye [20] it is difficult to estimate the uncertainty on these measurements. Here an uncertainty of 2% was assumed. An uncertainty in the inlet velocity profile will lead to an uncertainty of the transfer coefficients. Finally the deviations between measurements and simulations can be the result of flaws in the measurement setup such as defects in the insulation or an incorrect positioning of the sensors. This is however hard to check and will not be considered here.

The good agreement between the predicted temperature at various depths and the measured temperature clearly shows that the boundary conditions are correctly implemented.

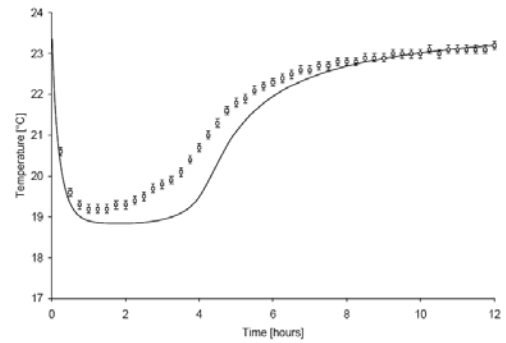


Figure 5 Temperature at 10mm

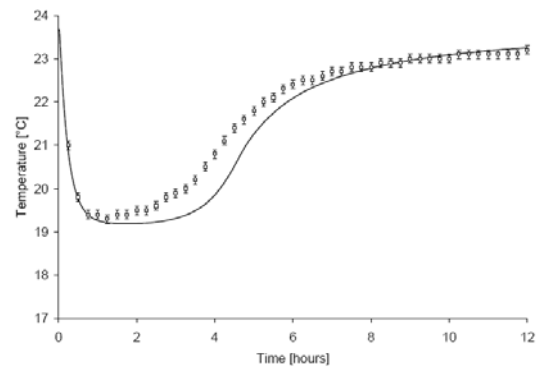


Figure 6 Temperature at 20mm

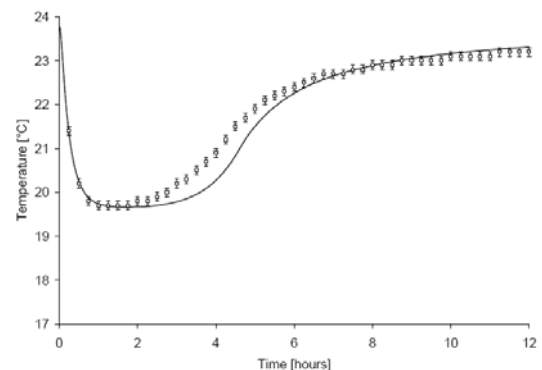


Figure 7 Temperature at 30mm

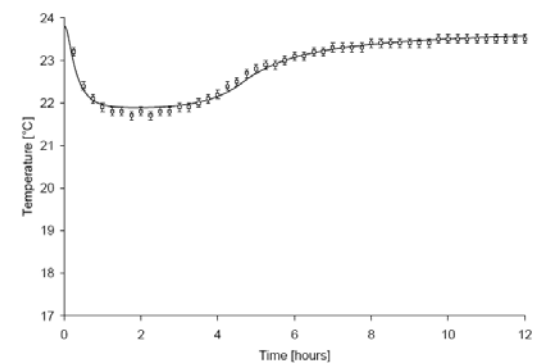


Figure 8 Temperature at 40mm

CONCLUSION

In this paper a finite volume HAM model is discussed and validated. Experiments found in literature were used and a good agreement between the measurements and modelling results was found. The discrepancies between the experiments and the model were attributed to three causes. First the uncertainty of the material properties can have a significant impact on the modelling outcome. Secondly the deviations between measurements and simulations could be the result of flaws in the measurement setup such as defects in the insulation or an incorrect positioning of the sensors. This was however hard to check and was not considered in this study. Finally the correct implementation of the boundary conditions was found to be very crucial.

To evaluate the impact of the boundary conditions three simulations were performed. First only a cross section of the setup was simulated. The convective boundary conditions at the top were assumed constant. This resulted in a clear underestimation of the predicted temperatures in the brick and an overestimation of the constant drying rate period. Next a longitudinal section of the setup was modelled. The convective boundary conditions at the top were no longer assumed constant and a developing boundary layer was taken into account. This way the leading edge effect was incorporated which implies that the brick dries out faster at the leading edge where the boundary layers for heat and mass are thinner. Finally the drying experiment was modelled in its full complexity by using a 3D model with the insulation and plexiglass included in the computational domain. This resulted in a very good agreement between the simulations and the experiments and demonstrated the importance of a correct implementation of the boundary conditions in order to have a good prediction of drying phenomena.

APPENDIX A: MATERIAL PROPERTIES

Hygrothermal properties ceramic brick

The material properties of ceramic brick were experimentally determined by Derluyn et al. [25].

Table 1. Hygrothermal material properties ceramic brick

property	unit	Ceramic brick
ρ	[kg/m ³]	2087
c_p	[J/kgK]	840
λ	[W/mK]	1+0.0047w
μ_{dry}	[-]	24.79
w_{cap}	[kg/m ³]	130

w_{cap} is the capillary moisture content, μ_{dry} the dry vapour resistance factor. The vapour resistance factor is the ratio of the vapour diffusivity of the material to the vapour diffusivity of air.

Vapour diffusion coefficient

$$\delta = \frac{2.61 \times 10^{-5}}{\mu_{dry} R_v T} \frac{1 - (w/w_{cap})}{0.503(1 - (w/w_{cap}))^2 + 0.497} \quad (20)$$

T here is in Kelvin

Moisture retention curve

$$w(p_c) = w_{cap} \left[\frac{0.846 \left(1 + (1.394 \times 10^{-5} p_c)^4 \right)^{-0.75}}{0.154 \left(1 + (0.9011 \times 10^{-5} p_c)^{1.69} \right)^{-0.408}} + \right] \quad (21)$$

Liquid permeability

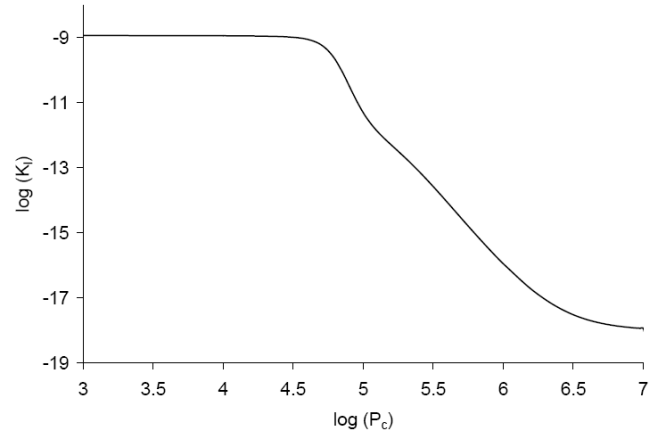


Figure 9. Liquid permeability of ceramic brick

Material properties PMMA and XPS

Table 2. Material properties PMMA and XPS

Property	Unit	PMMA	XPS
ρ	[kg/m ³]	1180	65
c_p	[J/kgK]	1500	1450
λ	[W/mK]	0.18	0.034

REFERENCES

- [1] Defraeye T., Blocken B., Derome D., Nicolai B., Carmeliet J., Convective heat and mass transfer modelling at air-porous material interfaces: Overview of existing methods and relevance, *Chemical Engineering Science* Vol. 74, 2012, pp. 49-58
- [2] McMinn W.A.M., Magee T.R.A., Principles, Methods and Applications of the Convective Drying of Foodstuffs, *Food and Bioproducts Processing*, Vol. 77, No. 3, 1999, pp. 175-193
- [3] Barati E., Esfahani J.A., Mathematical modeling of convective drying: Lumped temperature and spatially distributed moisture in slab, *Energy*, Vol. 36, No. 4, 2011 pp. 2294-2301
- [4] Landman K.A., Pel L., Kaasschieter E.F., Analytic modelling of drying of porous materials. *Mathematical Engineering in Industry*, Vol. 8, No. 2, 2001, pp. 89-122
- [5] Crank J., *The Mathematics of Diffusion*, Oxford University Press, Oxford, 1975.
- [6] Milly P.C.D., Moisture and heat transport in hysteretic, inhomogeneous porous media: a matrix head-based formulation and a numerical model, *Water Resources Research*, Vol. 18, No. 3, 1982, pp. 489-498
- [7] Wang N., Brennan J.G., A mathematical model of simultaneous heat and moisture transfer during drying of potato, *Journal of Food Engineering*, Vol. 24, No. 1, 1995, pp. 47-60
- [8] Hagetoft C.-E., Kalagasidis A.S., Adl-Zarrabi B., Roels S., Carmeliet J., Hens H., et al. Assessment Method of Numerical Prediction Models for Combined Heat, Air and Moisture Transfer in

- Building Components: Benchmarks for One-dimensional Cases, *Journal of Thermal Envelope and Building Science*, Vol. 27, No. 4, 2004, pp. 327-352
- [9] Hussain M.M., Dincer I., Two-dimensional heat and moisture transfer analysis of a cylindrical moist object subjected to drying: A finite-difference approach, *International Journal of Heat and Mass Transfer*, Vol. 46, No. 21, 2003, pp. 4033-4039
- [10] Le Page J.-F., Chevarin C., Kondjoyan A., Daudin J.-D., Mirade P.-S., Development of an approximate empirical-CFD model estimating coupled heat and water transfers of stacked food products placed in airflow, *Journal of Food Engineering*, Vol. 92, No. 2, 2009, pp. 208-216
- [11] Shokouhmand H., Abdollahi V., Hosseini S., Vahidkhal K., Performance Optimization of a Brick Dryer Using Porous Simulation Approach, *Drying Technology*, Vol. 29, No. 3, 2011, pp. 360-370
- [12] Masmoudi W., Prat M., Heat and Mass-Transfer between a Porous-Medium and a Parallel External Flow - Application to Drying of Capillary Porous Materials, *International Journal of Heat and Mass Transfer*, Vol. 34, No. 8, 1991, pp. 1975-1989
- [13] Amir H., Le Palec G., Daguene M., Séchage superficiel d'un matériau poreux humide par convection forcée d'air chaud: couplage entre les équations de transfert dans le matériau et celles de la couche limite, *International Journal of Heat and Mass Transfer*, Vol. 30, No. 6, 1987, pp. 1149-1158
- [14] Dolinskiy A.A., Dorfman A.S.H., Davydenko B.V., Conjugate heat and mass transfer in continuous processes of convective drying, *International Journal of Heat and Mass Transfer*, Vol. 34, No. 11, 1991, pp. 2883-2889
- [15] Defraeye T., Blocken B., Carmeliet J., Analysis of convective heat and mass transfer coefficients for convective drying of porous flat plate by conjugate modeling, *International Journal of Heat and Mass Transfer*, Vol. 55, 2012, pp. 112-124
- [16] Whitaker S., Simultaneous heat, mass and momentum transfer in porous media: A theory of drying, Academic Press, New York, 1977
- [17] Philip J.R., de Vries D.A., 1957. Moisture movement in porous materials under temperature gradients, *Transactions of the American Geophysical Union*, Vol. 38, 1957, pp. 222-232
- [18] Van Belleghem M., Ameel B., Janssens A., De Paepe M., Modelling heat and moisture transport in porous materials with CFD for building applications, *Proceedings of the 8th international conference on heat transfer, fluid mechanics and thermodynamics*, Pointe aux Piments, Mauritius, July 2011.
- [19] Van Belleghem M., De Backer L., Janssens A., De Paepe M. Development of a coupled CFD-HAM model including liquid moisture transport to study moisture transport in building materials, *5th International Building Physics Conference, IBPC2012*, Kyoto, Japan, April 2012.
- [20] Defraeye T., Convective Heat and Mass Transfer at Exterior Building Surfaces, PhD thesis, Leuven, KULeuven, 2011
- [21] Dean R.B., Reynolds Number Dependence of Skin Friction and Other Bulk Flow Variables in Two-Dimensional Rectangular Duct Flow, *Journal of Fluids Engineering*, Vol. 100, No. 2, 1978, pp. 215-223
- [22] Siegel R., Howell J.R., Thermal Radiation Heat Transfer, Hemisphere Publishing Corporation, Washington, 3th edition, 1992
- [23] Roels S., Talukdar P., James C., Simonson C.J., Reliability of material data measurements for hygroscopic buffering. *International Journal of Heat and Mass Transfer*, Vol.53, No. 23-24, 2010, pp. 5355-5363
- [24] Van Belleghem M., Steeman H.-J., Steeman M., Janssens A., De Paepe M., Sensitivity analysis of CFD coupled non-isothermal heat and moisture modelling. *Building and Environment*, , Vol. 45, No. 11, 2010, pp. 2485-2496
- [25] Derluyn H., Janssen H., Moonen P., and Carmeliet J., Moisture transfer across the interface between brick and mortar joint. *In Proceedings of the 8th Symposium on Building Physics in the Nordic Countries*, Copenhagen, Denmark, 2008.